PHYSICAL REVIEW A **105**, 042806 (2022)

Radiative force from optical cycling on magnesium monofluoride

Ruoxi Gu,[1] Kang Yan,[1] Di Wu,[1] Jin Wei,[1] Yong Xia,[1,2,3,*] and Jianping Yin[1,†]
[1]*State Key Laboratory of Precision Spectroscopy, School of Physics and Electronic Science,*
East China Normal University, Shanghai 200241, China
[2]*Collaborative Innovation Center of Extreme Optics, Shanxi University, Taiyuan, Shanxi 030006, China*
[3]*NYU-ECNU Institute of Physics at NYU Shanghai, Shanghai 200062, China*

(Received 30 December 2021; accepted 16 March 2022; published 13 April 2022)

We demonstrate radiative force deflection by using an optical cycling of the $X\,^2\Sigma^+_{1/2} - A\,^2\Pi_{1/2}$ electronic transition in diatomic molecule magnesium monofluoride (MgF). For the (0,0) and (0,1) bands of the electronic transition, the Franck-Condon factors—obtained by the dispersed laser-induced fluorescence spectrum—are $f_{00} = 0.972$ and $f_{01} = 0.028$, which suggests that the vibrational branching is quasiclosed. Furthermore, the dark Zeeman sublevels are destabilized by applying an external magnetic field. The cycling fluorescence is clearly observed to reveal that the molecular beam is deflected by 4.9 mm via scattering ∼200 photons per molecule. This work is encouraging toward laser cooling and magneto-optical trapping of MgF molecules.

DOI: 10.1103/PhysRevA.105.042806

I. INTRODUCTION

Great progress has been made in producing ultracold molecules that promise a powerful experimental platform for applications in precision measurement, ultracold collision and chemistry, complex quantum systems under precise control [1–3]. In the past decade, direct laser cooling techniques have been applied to diatomic molecules, such as SrF [4], YO [5], CaF [6,7], YbF [8], BaH [9], BaF [10,11], AlF [12], and CH [13], as well as polyatomic molecules, such as $CaOCH_3$ [14], SrOH [15], YbOH [16], and CaOH [17]. Magneto-optical traps of diatomic molecules have realized [6,7,18–20]. The 3D blue-detuned molasses has been reported to enable further cooling CaF and SrF down to 50 μK [6,21,22], which is well below the Doppler limit. Recently, YO molecules trapped in a 1D optical lattice were cooled down to 1 μK [23]. For laser cooling of molecules, in general the first step is to establish a closed optical cycling, providing continuous scattering of photons. To verify the optical cycling, one measures the deflection of molecular beam by radiation pressure. The number of photons scattered by molecules can be obtained from the deflection distance, by which the scattering rate can be estimated. The deflection of molecular beam was reported first by DeMille and co-workers [24]. The SrF beam was deflected by ∼0.5 mm (where the deflection region and probe region are separated by D = 12.5 cm) via scattering ∼140 photons, indicating that the scattering rate is 3 MHz. Then in 2017, Yan, *et al.* demonstrated the radiative force from ∼150 scattered photons on BaF beam leading to an ∼0.8 mm deflection (where $D = 35$ cm), and the scattering rate is ∼2 MHz [10]. The deflection on BaH was reported as ∼1 mm (where D is longer than 75 cm), consistent with scattering ∼80 photons per molecule at the average rate of 0.8 MHz [25]. Further, the scattering rate of AlF was measured as ∼23 MHz by ∼55 scattered photons—a displacement of ∼2.15 mm (where $D = 28$ cm) [26]. The radiative force deflection was also reported on triatomic molecules, such as SrOH [27].

Our laboratory suggests MgF molecule is another good candidate for laser cooling experiment due to the following characteristics [28]: (i) a strong spontaneous radiation decay ($\Gamma = 2\pi \times 22$ MHz) and a relatively large scattering force with lighter mass; (ii) the highly diagonalized Franck-Condon factors (FCFs); (iii) the simple hyperfine structure. So, laser cooling of MgF has been studied experimentally and theoretically in details [28–33]. The laser cooling relevant transitions of $X\,^2\Sigma^+_{1/2}$ $(v = 0,\ 1,\ N = 1)$ to $A\,^2\Pi_{1/2}$ $(v' = 0,\ J' = 1/2)$ were measured [31]. To prove that the vibrational branching is closed, the accurate FCFs must be determined. The FCFs mean the overlap between the vibrational wave functions upon electronic transition and are proportional to the square of the integral between the vibrational wave functions of the two electronic states. Molecules that have highly diagonal FCFs are prone to be cooled because many photons will be scattered on that transition. We have calculated the FCFs associated with 0-0 band—f_{00}—which is greater than 0.997 [28]. In particular, the FCFs were calculated by combining the spectroscopic constants from several different papers. The constants for the $X\,^2\Sigma^+_{1/2}$ state were taken from the experimental work which was recorded at a resolution of 0.01 cm^{-1} [34]. The constants for the $A\,^2\Pi_{1/2}$ state came from Ref. [35] that presents a compilation of data from various studies. There are some differences in the molecular constants among different papers [36–38]. The selection of constants has a significant influence on the calculated FCFs. Besides, rotational constant B_e for the $A\,^2\Pi_{1/2}$ state in MgF has never been determined explicitly. Vibrational constant ω_e corresponds to $\Delta G_{1/2}$ which is not the real ω_e for the $A\,^2\Pi_{1/2}$ state. In other words, there is no complete set of constants for calculate FCFs.

---

[*] yxia@phy.ecnu.edu.cn
[†] jpyin@phy.ecnu.edu.cn

2469-9926/2022/105(4)/042806(9)

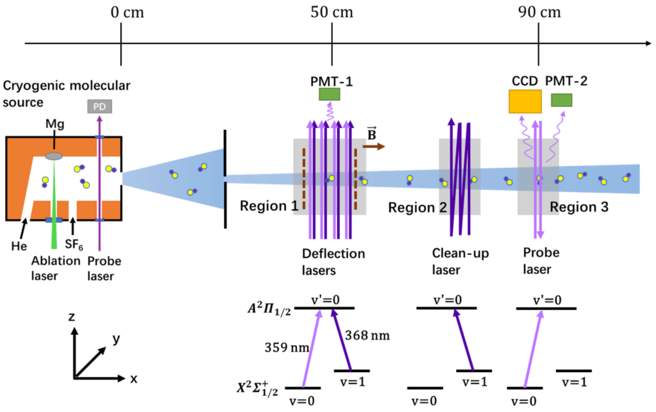

FIG. 1. Schematic of the experimental setup (distance is not scaled). The cryogenic MgF molecular beam is generated by chemical reaction and laser ablation, followed by buffer gas cooling with 4.6 K helium gas. The light purple color represents the pump laser at 359 nm while the deep purple color represents the repump laser at 368 nm. The laser polarization is on the xz plane. To remix Zeeman dark states, a magnetic field whose direction is along the x-axis is applied in region 1. In region 2, clean-up laser pumps the molecules from the $X(v=1)$ state back to the $X(v=0)$ state. In region 3, molecular beam profile is imaged by a CCD camera. There are two PMTs collecting LIF signal in region 1 and 3. To cover the hyperfine energy levels, all the lasers are modulated by EOMs.

In this work, solid FCFs are obtained based on the high resolution rovibrational spectra of the $A\,^2\Pi_{1/2}-X\,^2\Sigma^+_{1/2}$ transition in MgF cooled in buffer gases. After verifying that the vibrational branch is quasiclosed, a sideband modulation is employed to cover the hyperfine levels while an external magnetic field is used to remix dark Zeeman sublevels. So, the optical cycling is verified by the change of the cycling laser-induced fluorescence (LIF) signal. The resulting radiation pressure force from ∼200 scattered photons produces a ∼4.9 mm deflection.

II. EXPERIMENTAL SETUP

The experimental apparatus has been described in previous publications [30]. In short, it is shown schematically in Fig. 1. Gas-phase MgF is produced by the laser ablation and is entrained from a cryogenic buffer-gas chamber. In comparison with our previous work, the cryogenic source cell has now reached 4.6 K by optimizing thermal contact between the cool head and cryogenic chamber. After exiting from the cryogenic cell, a mixture of MgF and He pass through a rectangular 2 mm × 1.5 mm slit to be collimated transversely. The room temperature apparatus consists of 3 regions, namely interaction, clean-up and probe regions. Region 1 is located 50 cm downstream from the cell exit. The distance between regions 1 and 3 is $D=40$ cm. Time-of-flight (ToF) signal can be obtained by collecting the LIF with each photomultiplier (PMT) in regions 1 and 3. Besides, the LIF signal from a transverse retroreflected probe laser in region 3 is also collected by a CCD camera to record the molecular beam profiles. In front of the PMTs and CCD, band-pass filters are used to minimize the background light. Using the ToF signal collected in regions 1 and 3, the most probable forward velocity of MgF molecular beam is measured to be 450 m/s. Considering the beam forward velocity and the laser beam size, we can estimate molecule-light interaction time.

For different experimental purposes, there are different light path to achieve corresponding interactions. Fig. 1 shows the light path used to observe deflection through radiative force of MgF molecular beam. In this scheme, four passes of deflection laser are applied perpendicular to the molecular beam propagation in region 1. The main v_{00} pump (359 nm) and v_{10} repump (368 nm) laser are overlapped spatially to exert deflection. Both have linear polarization with 115 MHz sidebands generated by electro-optic modulators (EOM) to nearly excite all the hyperfine transitions in $X(v=0,\ 1,\ N=1)-A(v'=0,\ J'=1/2)$. The diameter and power of pump or repump laser are 5 mm and 400 mW, respectively. To remix the dark Zeeman sublevels, a pair of Helmholtz coils is used to generate a magnetic field of 16 Gs at an angle of 60 ° relative to the laser polarization. In region 2, a clean-up laser, split from the repump laser, is applied to repump the molecular population from the $X(v=1)$ back to the $X(v=0)$ to enhance the signal, which involve multiple passes. In region 3, the probe laser at 359 nm, produced from a separate laser source, is locked on the frequency of the $X(v=0,\ N=1)-A(v'=0,\ J'=1/2)$ transition. The 115 MHz sidebands are added to the probe laser.

The lasers in this work are produced from frequency doubling a CW Ti:sapphire laser, which has a large tuning range (700–1030 nm) and a narrow linewidth (less than 10 MHz) [39]. The laser frequency is locked to a highly stable reference resonator, which still allows to be scannable by scanning the reference cell. The fundamental frequencies of all the lasers are stabilized to the readout of a wavemeter (HighFinesse WS-U) that is calibrated by the Cesium D$_1$ line.

III. RESULTS AND ANALYSIS

A. FCFs of the $X\,^2\Sigma_{1/2}$ and $A\,^2\Pi_{1/2}$ states

To obtain the molecular constants for predicting FCFs, we first measure the spectra for the (0,0), (0,1), and (1,1) bands of the $A\,^2\Pi_{1/2}-X\,^2\Sigma^+_{1/2}$ electronic transition. For the (0,0) vibrational band, we observed the P, Q, R transitions in region 1 directly because of the majority population in the $X\,^2\Sigma^+_{1/2}$ $(v=0)$ state and the large f_{00}. For the (0,1) vibrational band, a pump laser in region 1 drives the $A\,^2\Pi_{1/2}(v'=0)-X\,^2\Sigma^+_{1/2}$ $(v=0)$ transition to pump the molecules out of the $X(v=0)$ state and into the $X(v=1)$ state. Because f_{00} is much larger than f_{01}, which means most molecules will decay back to the $X\,^2\Sigma^+_{1/2}$ $(v=0)$ state after being pumped to the $A\,^2\Pi_{1/2}(v'=0)$ state, the cleanup laser in region 2 can repump molecules back to v = 0 by driving the $A\,^2\Pi_{1/2}$ $(v'=0)-X\,^2\Sigma^+_{1/2}$ $(v=1)$ transition. Then, a probe laser, in resonance with the transition $A\,^2\Pi_{1/2}(v'=0)-X\,^2\Sigma^+_{1/2}$ $(v=0)$, detects the population in v = 0 in region 3. In the process, the frequency of the repump laser is scanned around 368.7 nm. Once the repump laser resonates with (0,1) transition, PMT-2 in region 3 will detect the population in the $X\,^2\Sigma^+_{1/2}$ $(v=0)$ state. Note that frequencies of the pump and the probe laser should be adjusted

TABLE I. Molecular constants (in cm^{-1}) for the $X\,^2\Sigma^+_{1/2}$ state and the $A\,^2\Pi_{1/2}$ state in MgF.

	$A\,^2\Pi_{1/2}$				
	T_e	$\omega_e{}'$	$B_e{}'$	$\alpha_e{}'$	$\omega_e\chi_e{}'$
This work	27836.2580(12)	739.4918(24)	0.52889(11)[b]	0.00477(18)	3.00091(50)
[37]	27847.4; 27813.1	746			
[38]	27829.60	740.12			
	$X\,^2\Sigma^+_{1/2}$				
		ω_e	B_e	α_e	$\omega_e\chi_e$
This work		717.49450(51)	0.51926(12)	0.00484(20)	5.90911(50)
[37]		718.2			
[38]		721.6	0.51922	0.00470	4.94
[43][a]			0.519272	0.004717	
[34]		720.1404	0.51927251	0.00471745	4.2602

[a] Here, the MHz unit in Ref. [43] is converted to cm^{-1} for comparison's purpose.

[b] The spectroscopic constants of the $A\,^2\Pi$ state of MgF has been reported recently [44]. There is one constant that can be compared with this work, which is B'_0 of $A\,^2\Pi$ state. B'_0 in our work can be calculated as $B'_0 = B'_e - \alpha'_e(v + \frac{1}{2}) = 15784.2\,\text{MHz}$, which is close to the value (15788.2 MHz) in Ref. [44].

to the corresponding rotational branch in circumstances of determining different rotational branches of (1,0) band.

For the (1,1) vibrational band, the pump laser still aims to pump the population from $v = 0$ to $v = 1$. Different from the laser configuration of (0,1) band, the repump laser is not needed in region 2 and the frequency of the probe laser is scanned around 359 nm that is the frequency of the $A\,^2\Pi_{1/2}(v' = 1) - X\,^2\Sigma^+_{1/2}$ $(v = 1)$ transition, which is because the f_{11} is much larger than f_{10}. The main purpose of the addition of lasers is to prepare the population in the state we need. Another function of the pump laser is to distinguish the $A\,^2\Pi_{1/2}$ $(v' = 1) - X\,^2\Sigma^+_{1/2}$ $(v = 1)$ transitions from the $A\,^2\Pi_{3/2}$ $(v' = 0) - X\,^2\Sigma^+_{1/2}$ $(v = 0)$ transitions because of some overlap between them. If the addition of v_{00} pump laser makes the LIF signal increase, then this rotational line is of the $A\,^2\Pi_{1/2}$ $(v' = 1) - X\,^2\Sigma^+_{1/2}$ $(v = 1)$ transition.

The frequencies of the rotational line positions of the $A\,^2\Pi_{1/2} - X\,^2\Sigma_{1/2}$ (0,0), (1,0) and (1,1) bands are listed in Appendix, along with the difference between the observed and calculated frequencies and the quantum number assignments. The calculated frequencies are obtained by use of our new fitted parameters and the detailed calculation are introduced below.

Combining the vibration and the rotation degrees of freedom, the rovibrational energy could be expressed as a double power series as [40]

$$E_{v,J} = \sum_{k\ell} Y_{k\ell}\left(v + \frac{1}{2}\right)^k [J\,(J+1) - \Lambda^2]^\ell, \qquad (1)$$

with $\Lambda = 0$ $(\Lambda = 1)$ for the $X\,^2\Sigma^+$ $(A\,^2\Pi)$ state, where v and J are the vibrational and rotational quantum numbers. The Dunham coefficients $Y_{k\ell}$ in Eq. (1) and the standard spectroscopic parameters are closely related according to the following:

$$Y_{10} \approx \omega_e,\ Y_{20} \approx -\omega_e x_e,\ Y_{01} \approx B_e,\ Y_{11} \approx -\alpha_e. \qquad (2)$$

For the $A\,^2\Pi$ state, taking the Λ-doubling into account, because the $A\,^2\Pi$ state has been proved to be a normal state [30], additional terms are added to the customary Dunham expansion. The energy of the $A\,^2\Pi_{1/2}$ state can be expressed as [41]

$$E'_{vj} = \sum_{k\ell} Y_{k\ell}\left(v + \frac{1}{2}\right)^k [J(J+1) - \Lambda^2]^\ell - B'_v\sqrt{\left(J' + \frac{1}{2}\right)^2 - \frac{A}{B_v{}'}\left(1 - \frac{A}{4B'_v}\right)}, \qquad (3)$$

where B_v and A corresponds to the molecular rotational constant and the spin orbit coupling constant, respectively. A is $36.406\,\text{cm}^{-1}$ obtained by our previous experimental work [30]. The transitions of the A-X states can be expressed by

$$\nu = T_e + E'{}_{vj} - E_{vj}. \qquad (4)$$

Using the energy expressions above, the experimental spectral lines are fitted by a nonlinear least-squares analysis. Table I presents the new fitting constants obtained from our spectral data, accompanied by the previous experimental results. We first complement the molecular constants for the $A\,^2\Pi_{1/2}$ state and give a set of parameters for the $A\,^2\Pi_{1/2}$ $-$ $X\,^2\Sigma^+_{1/2}$ transition, which has an important reference value for laser cooling.

Based on the measured molecular constants in Table I, we estimate the FCFs of the $A\,^2\Pi_{1/2}$ $- X\,^2\Sigma^+_{1/2}$ transition by using the method of the Rydberg-Klein-Rees (RKR) inversion [42]: the result is that $f_{00} = 0.9711$, $f_{01} = 0.0282$, and $f_{02} = 0.000726$.

To verify the calculated FCFs, we use a monochromator to record the dispersed laser-induced fluorescence spectrum from excitation of the $P_{11}(1)$ branch. The spectrum is scanned using a 0.06 nm step size for the scanning monochromator and averaging 20 ablation pulses per step. The LIF signal is collected in region 1 while PMT-2 in region 3 records LIF excited from the same laser to eliminate the fluctuation of

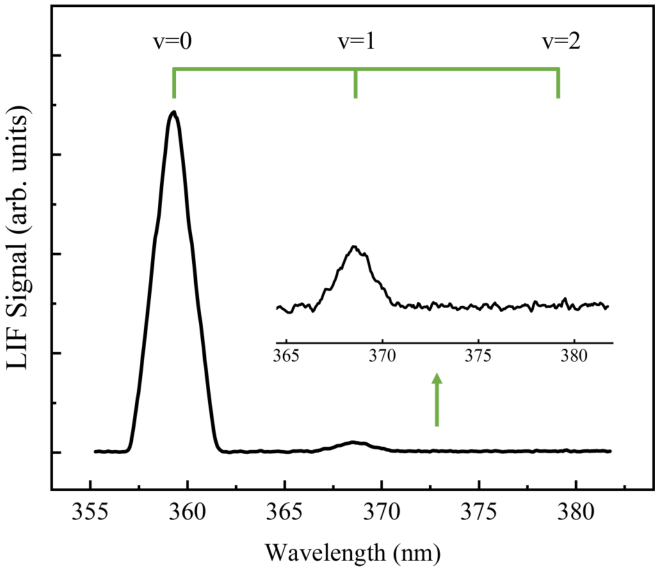

FIG. 2. Dispersed LIF spectrum of the $P_{11}(1)$ branch of the $A\,^2\Pi_{1/2}$ $(v' = 0) - X\,^2\Sigma^+_{1/2}$ $(v = 0)$ transition. The inset indicated by the green arrow is the magnified section for 365–382 nm.

molecular source. The spectrum is also recorded under the same conditions but without MgF molecular beam that can be achieved by blocking the ablation laser to remove the background light. In Fig. 2, we calculate the integrated areas of the LIF spectrum to obtain $f_{vv'}$ that are $f_{00} = 0.972$, $f_{01} = 0.028$. Note that the v_{02} transition is too small to resolve in the spectrum. The experimental result is in good agreement with the calculated one. So, we can efficiently cover the vibrational levels by using one pump laser and two repump lasers to obtain more than 50 000 scattered photons.

B. Optical cycling and radiative deflection

To construct a quasicycling transition to scatter more photons, all loss mechanisms should be addressed. In this section, we present the following feasibility of creating a cycling transition in MgF.

Firstly, the frequencies of the v_{00} and v_{10} laser with sideband modulation need to be determined because of the addition of EOM and the different excitation rates for different hyperfine levels. The lasers are locked on the position where the LIF signal was maximal. Figures 3(a) and 3(b) illustrates the dependence of LIF signal intensity on the frequency of the center frequency ν_0 without and with the sideband modulation, respectively. The black dots show the experimental LIF signal while the red curve represents the calculated LIF signal. The average number of photons emitted from the excited states are calculated by solving OBE to acquire relative intensities of spectra [45]. When the 115 MHz sideband modulation is on, three frequency components centered on ν_0, as shown in the purple line, interact with molecules together. If the frequency is scanned, three frequency components interact with the hyperfine energy levels in turn. For example, the first peak on the left represents the effect of the $(\nu_0 + 115)$ MHz component on the $F = 2$, $1+$ state. Here, we label the maximum LIF position—the detuning is 0 MHz. The frequency of v_{10} laser is determined in the same way.

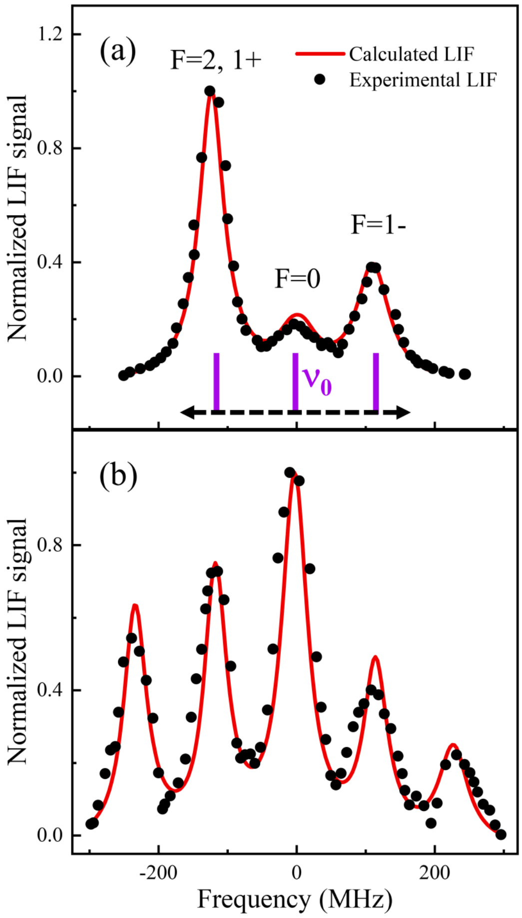

FIG. 3. Experimental LIF spectra in black dots and theoretical spectra by solving OBE in red curve: (a) without and (b) with EOM sideband adding to the pump laser. The purple vertical solid lines represent the center frequency ν_0, and the ±115 MHz sidebands of pump laser whose frequencies are scanned. The zero detuning is positioned where LIF is maximum and the frequency of pump laser is locked on this position.

The energy-level structures for the optical cycling of MgF are shown in Fig. 4(a). For the leakage channels in the $X(v = 0)$ state, we apply magnetic field and two EOMs to eliminate the Zeeman dark states and cover the hyperfine structures. In Figs. 4(b)and 4(c), we demonstrate an increase in LIF from spontaneously scattering photons by sequentially adding the conditions for photon cycling. Figure 4(b) gives the observed LIF enhancement due to photon cycling from the main pump transition in region 1. During this detection, one pass of lasers is through region 1. The LIF signal in this figure is collected by averaging 20 ablation pulses. The solid yellow curve shows the ToF signal with only the $P_{11}(1)$ line is addressed, that is to say, without any kind of dark states eliminated. The addition of $B = 16$ Gs (oriented at angle $\theta_B = 60^\circ$ relative to the linear laser polarization) enhances the LIF by a factor of ∼2.6, as shown by the dashed red curve. The setup of the magnetic field has been studied in our previous work [32]. The enhancement results from the destabilization of the extra two Zeeman dark sublevels labeled in short red lines in

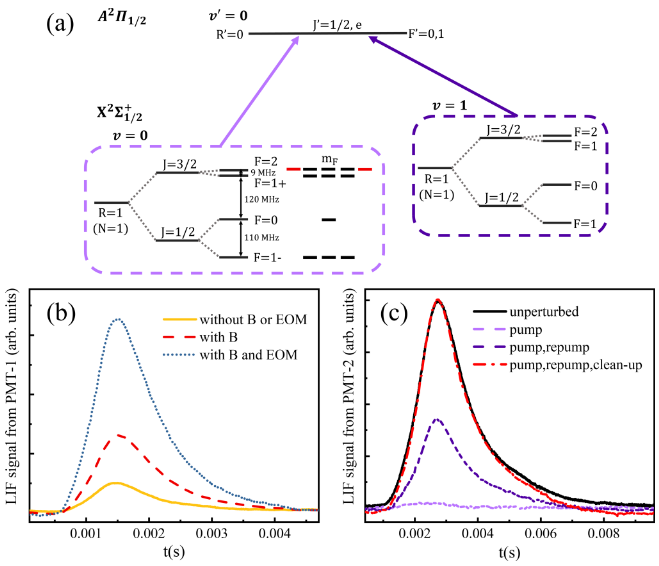

FIG. 4. (a) Energy-level structure related to optical cycling. The $X(v=0) - A(v'=0)$ transition is circled in dash light purple on the left. Inside, the short lines represent Zeeman sublevels m_F, and the six lines on the top can be excited when the pump laser is tuned to the frequency of the $X(v=0,\ N=1,\ F=2, 1+) - A(v'=0,\ J'=1/2)$ transition. The two red lines are remixed by the addition of magnetic field and the other four lines are covered by adding sideband modulation. The $X(v=1) - A(v'=0)$ transition is circled in dash deep purple box on the right. (b) ToF signals excited by one laser beam demonstrating cycling fluorescence from the main pump transition, collected in region 1. (c) ToF signals with four laser beams representing the population in the $X(v=0, N=1)$ state, collected in region 3.

Fig. 4(a). Further adding the 115 MHz sideband modulation, the fluorescence signal in dotted blue curve increases to ~6.6 times the yellow one. Now, all the hyperfine levels with the sublevels in the $X\,^2\Sigma^+_{1/2}(v=0, N=1)$ ground state can be addressed, which leads to more scattered photons before the molecules accumulate in the $X\,^2\Sigma^+_{1/2}(v=1)$ state.

Then, we solve the 4+13 multilevel optical Bloch equations (OBE) to do prediction, which shows that the elimination of Zeeman dark states is expected to enhance the LIF signal by a factor of ~3.0. The addition of sideband modulation can lead to about 6.8× increase of the scattered photon number per molecule, which is in good agreement with our experimental results.

The 4+13 theoretical model provides that with the interaction of pump laser, assuming sufficient interaction time, each molecule scatters about 34 photons, which is close to the predicted value of

$$N_{00} = \frac{1}{1 - f_{00}} \approx 36. \tag{5}$$

So, we close the hyperfine and spin-rotation splitting of MgF and cycle close to more than 30 photons per molecule.

Another leakage channel is the decay to the first vibrational ground state, $X\,^2\Sigma^+_{1/2}(v=1)$. To achieve enough scattered photons, the repump laser of v_{10} is crucial. Figure 4(c) proves the great effect of repump laser and cleanup laser. The ToF signal collected in region 3, representing the population in the $X\,^2\Sigma^+_{1/2}(v=0, N=1)$ state, is recorded by averaging 20 ablation pulses for an unperturbed molecular beam (black curve) and with different interaction laser on. Besides, we use four passes of laser beams with sideband modulation as well as a magnetic field to check the function of the interaction lasers in deflection experiment. The 359 nm pump laser almost depletes all the molecules in the $X\,^2\Sigma^+_{1/2}(v=0, N=1)$ state, so no population is detected by the probe laser locked to the frequency of $A\,^2\Pi_{1/2}(v'=0,\ J'=1/2) - X\,^2\Sigma^+_{1/2}(v=0,\ N=1)$, as shown by the dashed light purple (the lowest) curve. Application of the 368 nm repump laser in region 1 returns molecules to the ground vibrational level, so to increase signal seen as the dashed deep purple curve. Then, the application of the clean-up laser (in region 2) recovers the signal as seen in the chain dotted red curve. In short, such dynamic curves show the choice of our schemes is effective.

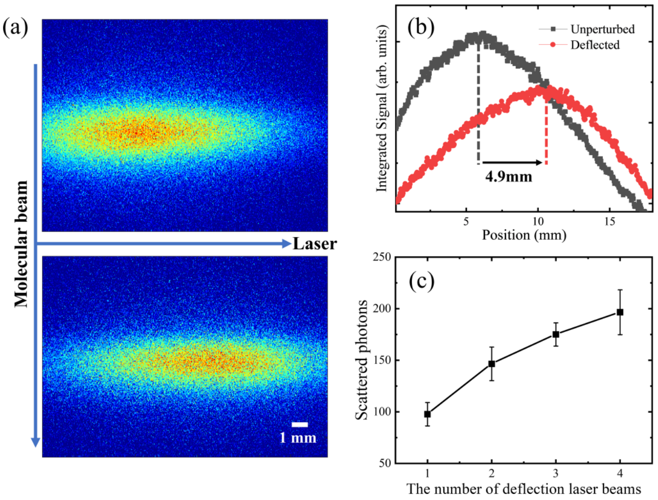

FIG. 5. Deflection of the MgF molecular beam due to optical cycling. (a) Image of the molecular beam passing through the probe laser beam with the deflection laser off (top) and on (bottom). (b) Integrated signal along the $\hat{x}$ axis. The black square one is from unperturbed and the red circle one is from deflected. The deflection distance is ~4.9 mm, indicated by the black arrow. (c) Number of scattered photons as a function of the number of laser beams.

After establishing the optical cycling scheme, it is expected to achieve the deflection of the MgF molecular beam using the radiation pressure force, which is a direct method to determine the number of scattered photons. Figures 5(a) and 5(b) show difference between the unperturbed and the deflected molecules in region 3. The images are integrated and fitted with a Gaussian to determine the deflection distance of $d \approx 4.9$ mm. The number of scattered photons N_{scat} can be estimated from the observed deflection. For MgF, the photon recoil velocity can be calculated by

$$v_{\text{recoil}} = \frac{h}{M\lambda} = 25.9 \text{ mm/s}, \tag{6}$$

where M is the mass of MgF and λ is the wavelength of the v_{00} transition. Therefore, the number of scattered photons can be obtained by the deflection distance as

$$N_{\rm scat} = \frac{d}{D}\frac{v_{\rm forward}}{v_{\rm recoil}} \approx 200. \qquad (7)$$

Besides, we measured the $N_{\rm scat}$ as a function of the number of laser beams, as Fig. 5(c) shows. The number of laser passes reflects the molecule-light interaction time. However, considering the fact that there exists inevitable loss of laser power resulting from two windows whose transmittance are 85% in the chamber of region 1, and the divergence and directivity of the molecular beam resulting from the deviation of vacuum system affect the interaction between laser and molecules, we can only make the most of the first pass of deflection laser in practice. Therefore, we consider the $N_{\rm scat}$ under the first deflection laser here, and the interaction time is 11 μs. The number of scattered photons is predicted to be $(N_{\rm scat})_{\rm OBE} \approx 105$ by solving OBE, in comparison of our experiment for one deflection laser is $98 \approx 0.93\ (N_{\rm scat})_{\rm OBE}$. Assuming that the intensity of laser is a constant (400 mW) in the whole interaction length ($d = 5$ mm), the scattering rate is estimated as $\Gamma_{\rm scat} = 9$ MHz. Considering that the maximum scattering rate is expressed by

$$\Gamma_{\rm max} = \frac{n_e}{n_e + n_g}\frac{1}{\tau} = \frac{4}{28}\Gamma, \qquad (8)$$

the scattering rate estimated by our experimental result is $\sim\Gamma_{\rm max}/2$. The reason why the scattering rate is not as large as $\Gamma_{\rm max}$ is probably that the distribution of laser intensity is actually uneven, which causes the inaccuracy of estimation. Besides, the sideband modulation inevitably leads to the different detuning from the hyperfine transitions of MgF, which may have an impact.

IV. CONCLUSION

In summary, we present the optical cycling for MgF molecule and the resulting deflection by radiation pressure force. We measure rovibrational spectra of the (0,0), (0,1), and (1,1) bands of the $A\,^2\Pi_{1/2} - X\,^2\Sigma^+_{1/2}$ transition and update the rotational constants to better calculate the FC factors by the RKR inversion. To check the Franck-Condon factors, we experimentally measure the FC factors as $f_{00} = 0.972$, $f_{01} = 0.028$, which are in good agreement with the theoretical ones. We apply the sideband modulation to cover the hyperfine transition and use the magnetic field to remix Zeeman dark sublevels, as manifested by the enhancement of LIF signal. At last, the MgF molecular beam is deflected by ~4.9 mm, indicating the number of scattered photons is ~200. To ignore the loss of laser intensity and instability of experimental system, we estimate the scattering rate by one pass of deflection laser beam as ~9 MHz. This work shows good promise for future laser cooling and magneto-optical trapping (MOT) of MgF molecule.

ACKNOWLEDGMENTS

We thank Hailing Wang and Lunhua Deng for many useful helps. We acknowledge the financial support from the National Natural Science Foundation of China under Grants No. 11834003, No. 91836103, and No. 12174115.

APPENDIX

The frequencies of the rotational line positions of the $A\,^2\Pi_{1/2} - X\,^2\Sigma_{1/2}$ (0,0), (1,0), and (1,1) bands are listed in Tables II and III, along with the difference between the observed and calculated frequencies and the quantum number assignments.

TABLE II. Observed and calculated transition frequencies of $A\,^2\Pi_{1/2} - X\,^2\Sigma^+_{1/2}$ (0,0) band of MgF (in GHz).

N	J	J'	$\upsilon_{\rm obs.}$	$\upsilon_{\rm cal.}$	$\upsilon_{\rm obs.} - \upsilon_{\rm cal.}$
			P_{11}		
1	1.5	0.5	834296.602	834296.601	0.001
2	2.5	1.5	834281.252	834281.250	0.002
3	3.5	2.5	834265.990	834266.017	−0.027
4	4.5	3.5	834250.864	834250.904	−0.040
5	5.5	4.5	834235.844	834235.913	−0.070
6	6.5	5.5	834220.986	834221.048	−0.062
7	7.5	6.5	834206.210	834206.311	−0.102
8	8.5	7.5	834191.628	834191.707	−0.079
9	9.5	8.5	834177.162	834177.239	−0.078
10	10.5	9.5	834162.874	834162.913	−0.039
11	11.5	10.5	834148.744	834148.734	0.010
12	12.5	11.5	834134.766	834134.708	0.058

TABLE II. (*Continued.*)

N	J	J'	$\upsilon_{\text{obs.}}$	$\upsilon_{\text{cal.}}$	$\upsilon_{\text{obs.}} - \upsilon_{\text{cal.}}$
Q_{11}					
0	0.5	0.5	834327.690	834327.627	0.063
1	1.5	1.5	834343.222	834343.272	−0.050
2	2.5	2.5	834359.092	834359.034	0.058
3	3.5	3.5	834374.910	834374.913	−0.004
4	4.5	4.5	834390.894	834390.912	−0.018
5	5.5	5.5	834407.012	834407.032	−0.021
6	6.5	6.5	834423.238	834423.276	−0.039
7	7.5	7.5	834439.666	834439.647	0.019
8	8.5	8.5	834456.200	834456.148	0.052
9	9.5	9.5	834472.888	834472.784	0.104
10	10.5	10.5	834489.742	834489.558	0.184
R_{11}					
0	0.5	1.5	834374.346	834374.297	0.048
1	1.5	2.5	834421.088	834421.056	0.032
2	2.5	3.5	834467.956	834467.930	0.025
3	3.5	4.5	834514.952	834514.922	0.030
4	4.5	5.5	834562.078	834562.031	0.047
5	5.5	6.5	834609.208	834609.261	−0.053
6	6.5	7.5	834656.520	834656.612	−0.092
7	7.5	8.5	834704.014	834704.088	−0.074
8	8.5	9.5	834751.626	834751.692	−0.067
9	9.5	10.5	834799.342	834799.429	−0.087
P_{12}					
2	1.5	0.5	834234.786	834234.721	0.065
3	2.5	1.5	834188.358	834188.431	−0.073
4	3.5	2.5	834142.312	834142.262	0.050
5	4.5	3.5	834096.296	834096.217	0.079
6	5.5	4.5	834050.366	834050.298	0.068
Q_{12}					
1	0.5	0.5	834296.766	834296.686	0.080
2	1.5	1.5	834281.428	834281.391	0.036
3	2.5	2.5	834266.166	834266.215	−0.049
4	3.5	3.5	834251.128	834251.159	−0.031
5	4.5	4.5	834236.182	834236.225	−0.043
6	5.5	5.5	834221.362	834221.417	−0.055
7	6.5	6.5	834206.656	834206.737	−0.081
8	7.5	7.5	834192.114	834192.189	−0.075
9	8.5	8.5	834177.680	834177.778	−0.098
10	9.5	9.5	834163.434	834163.509	−0.075
11	10.5	10.5	834149.362	834149.386	−0.024
12	11.5	11.5	834135.444	834135.417	0.027
R_{12}					
1	0.5	1.5	834343.422	834343.357	0.065
2	1.5	2.5	834359.262	834359.175	0.086
3	2.5	3.5	834375.168	834375.112	0.056
4	3.5	4.5	834391.162	834391.167	−0.006
5	4.5	5.5	834407.332	834407.344	−0.012
6	5.5	6.5	834423.662	834423.645	0.017
7	6.5	7.5	834440.058	834440.072	−0.014
8	7.5	8.5	834456.572	834456.630	−0.058
9	8.5	9.5	834473.314	834473.322	−0.008
10	9.5	10.5	834490.242	834490.154	0.088

TABLE III. Observed and calculated transition frequencies of $A\,^2\Pi_{1/2} - X\,^2\Sigma^+_{1/2}$ (1,0) and (1,1) bands of MgF (in GHz).

N	J	J'	$\upsilon_{\text{obs.}}$	$\upsilon_{\text{cal.}}$	$\upsilon_{\text{obs.}} - \upsilon_{\text{cal.}}$
$v = 1 - v' = 0$					
P_{11}					
1	1.5	0.5	812961.398	812961.410	−0.013
2	2.5	1.5	812946.618	812946.662	−0.044
3	3.5	2.5	812932.192	812932.316	−0.124
Q_{11}					
1	1.5	1.5	813008.100	813008.059	0.041
2	2.5	2.5	813024.528	813024.411	0.117
3	3.5	3.5	813041.192	813041.169	0.023
$v = 1 - v' = 1$					
P_{11}					
1	1.5	0.5	835130.760	835130.704	0.056
2	2.5	1.5	835115.598	835115.540	0.058
3	3.5	2.5	835100.492	835100.500	−0.008
4	4.5	3.5	835085.714	835085.589	0.125
Q_{11}					
0	0.5	0.5	835161.386	835161.402	−0.017
1	1.5	1.5	835176.958	835176.936	0.022
2	2.5	2.5	835192.574	835192.595	−0.022
3	3.5	3.5	835208.360	835208.383	−0.023
4	4.5	4.5	835224.284	835224.302	−0.018
R_{11}					
0	0.5	1.5	835207.584	835207.635	−0.051
1	1.5	2.5	835254.038	835253.992	0.046
2	2.5	3.5	835300.460	835300.478	−0.018
3	3.5	4.5	835347.058	835347.095	−0.038
P_{12}					
2	1.5	0.5	835069.240	835069.307	−0.067
3	2.5	1.5	835023.400	835023.445	−0.045

[1] J. Doyle, B. Friedrich, R. V. Krems, and F. Masnou-Seeuws, Eur. Phys. J. D **31**, 149 (2004).

[2] L. D. Carr, D. DeMille, R. V. Krems, and J. Ye, New J. Phys. **11**, 055049 (2009).

[3] D. S. Jin and J. Ye, Chem. Rev. **112**, 4801 (2012).

[4] E. S. Shuman, J. F. Barry, and D. DeMille, Nature (London) **467**, 820 (2010).

[5] M. T. Hummon, M. Yeo, B. K. Stuhl, A. L. Collopy, Y. Xia, and J. Ye, Phys. Rev. Lett. **110**, 143001 (2013).

[6] S. Truppe, H. J. Williams, M. Hambach, L. Caldwell, N. J. Fitch, E. A. Hinds, B. E. Sauer, and M. R. Tarbutt, Nat. Phys. **13**, 1173 (2017).

[7] L. Anderegg, B. L. Augenbraun, E. Chae, B. Hemmerling, N. R. Hutzler, A. Ravi, A. Collopy, J. Ye, W. Ketterle, and J. M. Doyle, Phys. Rev. Lett. **119**, 103201 (2017).

[8] J. Lim, J. R. Almond, M. A. Trigatzis, J. A. Devlin, N. J. Fitch, B. E. Sauer, M. R. Tarbutt, and E. A. Hinds, Phys. Rev. Lett. **120**, 123201 (2018).

[9] G. Z. Iwata, R. L. McNally, and T. Zelevinsky, Phys. Rev. A **96**, 022509 (2017).

[10] T. Chen, W. H. Bu, and B. Yan, Phys. Rev. A **96**, 053401 (2017).

[11] R. Albrecht, M. Scharwaechter, T. Sixt, L. Hofer, and T. Langen, Phys. Rev. A **101**, 013413 (2020).

[12] S. Truppe, S. Marx, S. Kray, M. Doppelbauer, S. Hofsäss, H. C. Schewe, N. Walter, J. Pérez-Ríos, B. G. Sartakov, and G. Meijer, Phys. Rev. A **100**, 052513 (2019).

[13] J. C. Schnaubelt, J. C. Shaw, and D. J. McCarron, arXiv:2109.03953.

[14] D. Mitra, N. B. Vilas, C. Hallas, L. Anderegg, B. L. Augenbraun, L. Baum, C. Miller, S. Raval, and J. M. Doyle, Science **369**, 1366 (2020).

[15] I. Kozyryev, L. Baum, K. Matsuda, B. L. Augenbraun, L. Anderegg, A. P. Sedlack, and J. M. Doyle, Phys. Rev. Lett. **118**, 173201 (2017).

[16] B. L. Augenbraun, Z. D. Lasner, A. Frenett, H. Sawaoka, C. Miller, T. C. Steimle, and J. M. Doyle, New J. Phys. **22**, 022003 (2020).

[17] L. Baum, N. B. Vilas, C. Hallas, B. L. Augenbraun, S. Raval, D. Mitra, and J. M. Doyle, Phys. Rev. Lett. **124**, 133201 (2020).

[18] J. F. Barry, D. J. McCarron, E. B. Norrgard, M. H. Steinecker, and D. DeMille, Nature (London) **512**, 286 (2014).

[19] A. L. Collopy, S. Ding, Y. Wu, I. A. Finneran, L. Anderegg, B. L. Augenbraun, J. M. Doyle, and J. Ye, Phys. Rev. Lett. **121**, 213201 (2018).

[20] N. B. Vilas, C. Hallas, L. Anderegg, P. Robichaud, A. Winnicki, D. Mitra, and J. M. Doyle, arXiv:2112.08349.

[21] L. Anderegg, B. L. Augenbraun, Y. Bao, S. Burchesky, L. W. Cheuk, W. Ketterle, and J. M. Doyle, Nat. Phys. **14**, 890 (2018).

[22] D. J. McCarron, M. H. Steinecker, Y. Zhu, and D. DeMille, Phys. Rev. Lett. **121**, 013202 (2018).

[23] Y. W. Wu, J. J. Burau, K. Mehling, J. Ye, and S. Q. Ding, Phys. Rev. Lett. **127**, 263201 (2021).

[24] E. S. Shuman, J. F. Barry, D. R. Glenn, and D. DeMille, Phys. Rev. Lett. **103**, 223001 (2009).

[25] R. L. McNally, I. Kozyryev, S. Vazquez-Carson, K. Wenz, T. Wang, and T. Zelevinsky, New J. Phys. **22**, 083047 (2020).

[26] S. Hofsäss, M. Doppelbauer, S. C. Wright, S. Kray, B. G. Sartakov, J. Pérez-Ríos, G. Meijer, and S. Truppe, New J. Phys. **23**, 075001 (2021).

[27] I. Kozyryev, L. Baum, K. Matsuda, H. Boerge, and J. M. Doyle, J. Phys. B At. Mol. Opt. Phys. **49**, 134002 (2016).

[28] L. Xu, Y. N. Yin, B. Wei, Y. Xia, and J. P. Yin, Phys. Rev. A **93**, 013408 (2016).

[29] S. P. Xu, M. Xia, R. X. Gu, Y. N. Yin, L. Xu, Y. Xia, and J. P. Yin, Phys. Rev. A **99**, 033408 (2019).

[30] S. P. Xu, M. Xia, Y. N. Yin, R. X. Gu, Y. Xia, and J. P. Yin, J. Chem. Phys. **150**, 084302 (2019).

[31] S. P. Xu, M. Xia, R. X. Gu, C. Y. Pei, Z. H. Yang, Y. Xia, and J. P. Yin, J. Quant. Spectrosc. Radiat. Transf. **236**, 106583 (2019).

[32] M. Xia, R. X. Gu, K. Yan, D. Wu, L. Xu, Y. Xia, and J. P. Yin, Phys. Rev. A **103**, 013321 (2021).

[33] K. Yan, B. Wei, Y. L. Yin, S. P. Xu, L. Xu, M. Xia, R. X. Gu, Y. Xia, and J. P. Yin, New J. Phys. **22**, 033003 (2020).

[34] B. E. Barber, K. Q. Zhang, B. Guo, and P. F. Bernath, J. Mol. Spectrosc. **169**, 583 (1995).

[35] K. P. Huber and G. Herzberg, *Molecular Spectra and Molecular Structure IV: Constants of Diatomic Molecules* (Van Rostrand-Reinhold, New York, NY, 2005).

[36] F. A. Jenkins and R. Grinfeld, Phys. Rev. **45**, 229 (1934).

[37] C. A. Fowler Jr, Phys. Rev. **59**, 645 (1941).

[38] R. F. Barrow and J. R. Beale, Proc. Phys. Soc. **91**, 483 (1967).

[39] Y. N. Yin, Y. Xia, X. J. Li, X. X. Yang, S. P. Xu, and J. P. Yin, Appl. Phys. Express **8**, 092701 (2015).

[40] J. L. Dunham, Phys. Rev. **41**, 721 (1932).

[41] G. Herzberg, *Molecular Spectra and Molecular Structure* (D. Van Nostrand, New York, NY, 1945).

[42] R. J. L. Roy, *Level 8.0, A Computer Program for Solving the Radial Schrodinger Equation for Bound and Quasibound Levels, Chemical Physics Research Report No. 663* (University of Waterloo, Waterloo, Ontario, 2007).

[43] M. A. Anderson, M. D. Allen, and L. M. Ziurys, Astrophys. J. **425**, L53 (1994).

[44] M. Doppelbauer, S. C. Wright, S. Hofsäss, B. G. Sartakov, G. Meijer, and S. Truppe, arXiv:2112.06555.

[45] R. X. Gu, M. Xia, K. Yan, D. Wu, J. Wei, L. Xu, Y. Xia, and J. P. Yin, J. Quant. Spectrosc. Radiat. Transf. **278**, 108015 (2022).